Integration Algorithm for Modeling the Elasto-Viscoplastic Response of Polycrystalline Materials

Gorti Sarma and Thomas Zacharia

Oak Ridge National Laboratory, Oak Ridge, TN 37831-6140, USA

September 21, 1998

Keywords: B. constitutive behavior, B. crystal plasticity, B. elastic-viscoplastic material, B. polycrystalline material, C. numerical algorithms

Abstract

An integration scheme is presented for modeling the texture evolution and stress-strain response of elasto-viscoplastic polycrystalline materials. Single crystal kinematics based on a multiplicative decomposition of the deformation gradient is used to obtain an evolution equation for the crystal elastic deformation gradient. An implicit scheme to integrate this equation is presented which is stable and efficient. The reorientation of the crystal as well as the elastic strain can then be obtained from a polar decomposition of the elastic deformation gradient. Numerical studies are presented using material parameters for aluminum (FCC crystals) and zircaloy (HCP crystals) to demonstrate the general nature of the model. Predictions of the model are also compared with those obtained using a rigid-viscoplastic polycrystal model which neglects the elastic response. Retaining the elastic response makes the model useful for large deformation analyses where both anisotropy due to texture as well as elastic effects such as springback and residual stresses are important.

1 Introduction

Metals have a polycrystalline microstructure, and over a broad range of processing conditions these polycrystals deform by shearing on crystallographic slip systems. Due to the limited number of available slip systems, a crystal accommodates an arbitrary deformation through a combination of slip and rotation. The preferential reorientation of crystals leads to texture, which is the main cause of anisotropy in the properties of the material (Kocks, 1987).

Simulating texture development and its impact on subsequent deformation requires material models which are capable of treating the distribution of crystal orientations and its evolution. Polycrystal models using the discrete aggregate representation of texture provide an effective means to address this challenge (e.g. Asaro and Needleman, 1985; Mathur and Dawson, 1989). Each material point is typically associated with a collection of single crystals, characterized by their orientations and slip system critical resolved shear stress (hardness) values. The material behavior is described by the collective response of the aggregate. By placing such an aggregate at each integration point of the finite element discretization of a deforming workpiece, it has been possible to model texture development during bulk deformation processes such as rolling, forging, sheet forming, etc. (Mathur and Dawson, 1989; Kalidindi *et al.*, 1992; Beaudoin *et al.*, 1994; Balasubramanian and Anand, 1996).

Two main modeling assumptions are required in the application of polycrystal models to predict the material behavior. The first is a relationship between the polycrystal and single crystal values of stress and/or strain. Various assumptions have been used for this purpose, the most common of which is the Taylor (1938) model, which assumes the deformation of each crystal to be homogeneous and equal to the macroscopic deformation. The model has been extended by Asaro and Needleman (1985) to accommodate rate dependent plasticity. The strict compatibility requirement of the Taylor assumption violates equilibrium at crystal boundaries. Nevertheless, it has been shown to give reasonably good texture predictions, especially for metals with high crystal symmetry and low rate sensitivity. Various other models have been proposed which relax the strict kinematic requirements of the Taylor hypothesis, such as the Sachs (1928) model, "relaxed" constraints approach (Kocks and Canova, 1981), and equilibrium-based theories (Chastel and Dawson, 1993). These models treat crystals as independent entities which do not interact with each other. Efforts to incorporate interaction among crystals have led to the "effective cluster" model (Kocks *et al.*, 1986), the modified Sachs model (Pederson and Leffers, 1987), and the "neighborhood compliance" model (Sarma and Dawson, 1996b).

The second main ingredient in polycrystal models is a constitutive description of the single crystal mechanical response. Some simulations of deformation processes have neglected the elastic response of the material, since the focus has been the prediction of texture development at large plastic strains (Mathur *et al.*, 1990; Beaudoin *et al.*, 1994), while others have included elasticity, with different approaches to the choice of integration schemes and variables (Peirce *et al.*, 1983; Kalidindi *et al.*, 1992; Maniatty *et al.*, 1992). These various models are based on a multiplicative decomposition of the deformation gradient into a plastic part which embodies isochoric plastic deformation by slip, and an elastic component which includes any rigid rotation of the lattice. The constitutive relations for elastic

and plastic response are expressed in the intermediate configuration obtained after plastic deformation. Peirce *et al.* (1983) used a hypoelastic description of elasticity along with an explicit update of the slip increments on each slip system. This model has also been used by Becker (1991a) to study deformation of single crystal and polycrystalline aluminum alloys. Kalidindi *et al.* (1992) have used an implicit integration scheme to model texture evolution during shear, torsion and forging of copper. Their integration procedure is based on updating the stress measure expressed in the intermediate configuration. Maniatty *et al.* (1992) have followed a similar approach based on a hyperelastic law which proceeds by integrating the plastic deformation gradient.

In this paper, we present an alternate and novel numerical scheme for integrating the constitutive equations for elasto-viscoplastic crystals that works directly with the evolution equation for the elastic deformation gradient. The motivation for choosing the elastic deformation gradient as the integration variable comes from the fact that it is the basis for defining both the elastic strain (which in turn is used to compute the stress) and the rigid rotation (which specifies the texture). In addition, the form of the evolution equation is well suited for problems where the deformation history of a material point is given in terms of its velocity gradient. This form of the equation is especially useful in a velocity based finite element formulation for simulating polycrystal deformation. The kinematic quantities are written in rate form, with the known or estimated velocity field being used to compute the velocity gradient at each integration point. One of the objectives for developing the elasto-viscoplastic model is its application to the study of residual stresses in polycrystalline materials using the finite element method. The choice of the elastic deformation gradient as the variable for integration results in a direct and simple method which is also quite general since it makes no simplifying assumptions. In the following sections, the constitutive assumptions based on single crystal kinematics are recalled, and the implicit integration scheme is described. Predictions of texture evolution and stress-strain response using the model for materials with FCC and HCP crystal structure are then presented.

In addition to the simulations of bulk deformation processes mentioned earlier, polycrystal models have also been applied at much smaller length scales (Dawson *et al.*, 1994) for detailed studies of polycrystal deformations. In these applications (e.g. Becker, 1991b; Bronkhorst *et al.*, 1992; Sarma and Dawson, 1996a; Beaudoin *et al.*, 1996), the finite element discretization is at the aggregate level, with several elements comprising each crystal. These simulations capture the inhomogeneities in deformation, not only across different crystals, but also within each crystal (Sarma *et al.*, 1998). Use of the model presented here with such detailed simulations at the microstructural scale will allow the computation of internal residual stresses in the polycrystal due to single crystal anisotropy and neighbor constraints.

A description of the notation used in the paper follows. Bold face lower and upper case letters indicate vectors (e.g. $\boldsymbol{b}$) and second order tensors (e.g. $\boldsymbol{L}$), respectively. Fourth order tensors are denoted by upper case bold calligraphic letters (e.g. $\boldsymbol{\mathcal{L}}$). A superimposed dot denotes material time derivative of that quantity. A superscript -1 indicates the inverse of a tensor, superscript T indicates its transpose, and superscript $-T$ indicates the transpose of its inverse. The inner product of two tensors is expressed as $\boldsymbol{A} \cdot \boldsymbol{B}$ and equals $A_{ij}B_{ij}$, with summation implied over repeated indices. The dyadic product of two tensors is expressed as

$\boldsymbol{A} \otimes \boldsymbol{B}$ and results in a fourth order tensor whose $ijkl$ component is given by $A_{ij}B_{kl}$. The product of two tensors $\boldsymbol{A}$ and $\boldsymbol{B}$ is denoted by $\boldsymbol{AB}$, with ij component $A_{ik}\,B_{kj}$. The result of a fourth order tensor $\boldsymbol{\mathcal{L}}$ operating on a second order tensor $\boldsymbol{A}$ is indicated by $\boldsymbol{\mathcal{L}}[\boldsymbol{A}]$, and leads to a second order tensor with ij component $\mathcal{L}_{ijkl}\,A_{kl}$. The second order identity tensor is written as $\mathbf{1}$, with ij component given by the Kronecker delta δ_{ij}. The symmetric fourth order identity tensor is written as $\mathfrak{S}$, with $ijkl$ component $\frac{1}{2}(\delta_{ik}\,\delta_{jl} + \delta_{jk}\,\delta_{il})$.

2 Description of Constitutive Model

Consider first the kinematics of a single crystal deforming from initial (or reference) configuration $\mathcal{B}_0$ to deformed configuration $\mathcal{B}$, as shown in Fig. 1. Following the approach of Lee (1969) and other researchers (Rice, 1971; Peirce *et al.*, 1983; Maniatty *et al.*, 1992; Kalidindi *et al.*, 1992) the deformation gradient $\boldsymbol{F}$ is written using a multiplicative decomposition as,

$$\boldsymbol{F} = \boldsymbol{F}^*\boldsymbol{F}^p, \qquad \det\,\boldsymbol{F}^p = 1, \qquad \det\,\boldsymbol{F}^* > 0, \tag{1}$$

where $\boldsymbol{F}^p$ is the plastic deformation gradient due to shearing along crystallographic slip planes, and $\boldsymbol{F}^*$ is the elastic deformation gradient which includes any rigid rotation of the lattice. The plastic deformation by slip is assumed to occur at constant volume, with the orientation of the lattice remaining unchanged. Rewriting equation (1) in rate form leads to the following expression for the velocity gradient,

$$\boldsymbol{L} = \dot{\boldsymbol{F}}\boldsymbol{F}^{-1} = \dot{\boldsymbol{F}}^*\boldsymbol{F}^{*-1} + \boldsymbol{F}^*\dot{\boldsymbol{F}}^p\boldsymbol{F}^{p-1}\boldsymbol{F}^{*-1} \tag{2}$$

The plastic part of the deformation gradient $\boldsymbol{F}^p$ is used to define a plastic velocity gradient $\tilde{\boldsymbol{L}}^p$, which is written relative to the intermediate configuration $\tilde{\mathcal{B}}$ as

$$\tilde{\boldsymbol{L}}^p = \dot{\boldsymbol{F}}^p\boldsymbol{F}^{p-1} = \sum_\alpha \dot{\gamma}^\alpha(\tilde{\boldsymbol{s}}^\alpha \otimes \tilde{\boldsymbol{m}}^\alpha) = \sum_\alpha \dot{\gamma}^\alpha \tilde{\boldsymbol{P}}^\alpha \tag{3}$$

The plastic velocity gradient is expressed as a linear combination of the slip system shearing rates $\dot{\gamma}^\alpha$. The dyadic product of the slip direction $\tilde{\boldsymbol{s}}^\alpha$ with the slip plane normal vector $\tilde{\boldsymbol{m}}^\alpha$ gives the Schmid orientation tensor $\tilde{\boldsymbol{P}}^\alpha$ in the intermediate configuration.

Constitutive assumptions must now be prescribed for the elastic and plastic deformation of the material. The elastic behavior is modeled using a constitutive law written in the intermediate configuration,

$$\boldsymbol{T}^* = \boldsymbol{\mathcal{L}}[\boldsymbol{E}^*] \tag{4}$$

where $\boldsymbol{\mathcal{L}}$ is a fourth order elasticity tensor. The strain measure is given by the Green strain tensor $\boldsymbol{E}^*$, defined in terms of the elastic deformation gradient $\boldsymbol{F}^*$ and the second order identity $\mathbf{1}$ as

$$\boldsymbol{E}^* = \frac{1}{2}\left(\boldsymbol{F}^{*T}\boldsymbol{F}^* - \mathbf{1}\right) \tag{5}$$

The corresponding stress measure which is elastic work conjugate to the Green strain is the second Piola-Kirchoff stress $\boldsymbol{T}^*$, given in terms of the Cauchy stress $\boldsymbol{T}$ by

$$\boldsymbol{T}^* = (\det\,\boldsymbol{F}^*)\boldsymbol{F}^{*-1}\boldsymbol{T}\boldsymbol{F}^{*-T} \tag{6}$$

The plastic deformation is modeled using a viscoplastic constitutive law to relate the shearing rate on each slip system $\dot{\gamma}^\alpha$ to its resolved shear stress τ^α. The use of a rate dependent model avoids the difficulty with possible non-uniqueness in choosing the active slip systems (Pan and Rice, 1983; Asaro and Needleman, 1985). The shearing rate is given by (Hutchinson, 1976; Pan and Rice, 1983)

$$\dot{\gamma}^\alpha = \dot{\gamma}_0 \left| \frac{\tau^\alpha}{\hat{\tau}^\alpha} \right|^{\frac{1}{m}} \operatorname{sign}(\tau^\alpha) \tag{7}$$

where m is the rate sensitivity parameter, $\dot{\gamma}_0$ is a reference rate of shearing, and $\hat{\tau}^\alpha$ is the critical resolved shear stress (hardness) on the slip system. The resolved shear stress is the component of the traction along the direction of slip, and is related to the Cauchy stress through the Schmid tensor as

$$\tau^\alpha = (\boldsymbol{T}\boldsymbol{m}^\alpha) \cdot \boldsymbol{s}^\alpha = \boldsymbol{T} \cdot (\boldsymbol{s}^\alpha \otimes \boldsymbol{m}^\alpha) \tag{8}$$

It is advantageous to rewrite the resolved shear stress in terms of the Schmid tensor in the intermediate configuration as

$$\tau^\alpha = (\boldsymbol{F}^{*T}\boldsymbol{F}^*\boldsymbol{T}^*) \cdot (\tilde{\boldsymbol{s}}^\alpha \otimes \tilde{\boldsymbol{m}}^\alpha) = (\boldsymbol{C}^*\boldsymbol{T}^*) \cdot \tilde{\boldsymbol{P}}^\alpha \tag{9}$$

The elastic deformation gradient tensor $\boldsymbol{F}^*$ contains information related to the reorientation of the crystal lattice as well as the elastic strain. Equations (2) and (3) can be combined to provide an expression for the evolution of $\boldsymbol{F}^*$,

$$\dot{\boldsymbol{F}}^* = \boldsymbol{L}\boldsymbol{F}^* - \boldsymbol{F}^*\tilde{\boldsymbol{L}}^p \tag{10}$$

The slip system hardness values are assumed to evolve with deformation according to a modified Voce-type hardening law (Kocks, 1976; Mathur and Dawson, 1989)

$$\dot{\hat{\tau}}^\alpha = H_0 \left\{ \frac{\hat{\tau}_s(\dot{\gamma}^*) - \hat{\tau}^\alpha}{\hat{\tau}_s(\dot{\gamma}^*) - \hat{\tau}_i^\alpha} \right\} \dot{\gamma}^* \tag{11}$$

where the hardening rate H_0 and the initial hardness $\hat{\tau}_i^\alpha$ are material parameters, and $\dot{\gamma}^*$ is the net shearing rate on all the slip systems,

$$\dot{\gamma}^* = \sum_\alpha |\dot{\gamma}^\alpha| \tag{12}$$

The saturation value of the hardness $\hat{\tau}_s$ based on the current slip system state is given by

$$\hat{\tau}_s(\dot{\gamma}^*) = \hat{\tau}_{s_0} \left(\frac{\dot{\gamma}^*}{\dot{\gamma}_s} \right)^{m'} \tag{13}$$

where $\hat{\tau}_{s_0}$, $\dot{\gamma}_s$ and m' are material parameters.

3 Integration Procedure

Given a deformation history in the form of the velocity gradient $\boldsymbol{L}$, the task now is to integrate the evolution equations (10) and (11), in order to determine the orientation, hardness, strain and stress in the crystal at any time. The deformation history is discretized into a number of time increments. The problem can be stated as follows:

> Knowing $\boldsymbol{F}^*$ and $\hat{\tau}^\alpha$ at time t, and given $\boldsymbol{L}$ at time $t + \Delta t$, find $\boldsymbol{F}^*$ and $\hat{\tau}^\alpha$ at time $t + \Delta t$.

The small values of rate sensitivity typical for metals make the evolution equation (10) highly non-linear. An implicit scheme is used in the computation of $\boldsymbol{F}^*(t + \Delta t)$, while keeping the value of $\hat{\tau}^\alpha$ fixed at its current value. This is expressed as

$$\boldsymbol{F}^*_{t+\Delta t} = \boldsymbol{F}^*_t + \Delta t\, \boldsymbol{L}_{t+\Delta t} \boldsymbol{F}^*_{t+\Delta t} - \Delta t\, \boldsymbol{F}^*_{t+\Delta t} \left(\sum_\alpha \dot{\gamma}^\alpha_{t+\Delta t} \tilde{\boldsymbol{P}}^\alpha \right) \tag{14}$$

The known quantities in equation (14) are $\boldsymbol{F}^*_t$, $\boldsymbol{L}_{t+\Delta t}$ and $\tilde{\boldsymbol{P}}^\alpha$. Using equation (7), the slip system shearing rates are given by

$$\dot{\gamma}^\alpha_{t+\Delta t} = \dot{\gamma}_0 \left(\frac{\tau^\alpha_{t+\Delta t}}{\hat{\tau}^\alpha_t} \right) \left| \frac{\tau^\alpha_{t+\Delta t}}{\hat{\tau}^\alpha_t} \right|^{\frac{1}{m}-1} \tag{15}$$

It is noted again that the hardness is assumed to remain constant over the time increment, and hence its value at time t is used in the above equation. The resolved shear stress is obtained from equation (9),

$$\tau^\alpha_{t+\Delta t} = (\boldsymbol{C}^*_{t+\Delta t} \boldsymbol{T}^*_{t+\Delta t}) \cdot \tilde{\boldsymbol{P}}^\alpha \tag{16}$$

where $\boldsymbol{C}^*_{t+\Delta t}$ and $\boldsymbol{T}^*_{t+\Delta t}$ can be expressed in terms of the unknown $\boldsymbol{F}^*_{t+\Delta t}$ using equations (9), (5) and (4),

$$\begin{aligned} \boldsymbol{C}^*_{t+\Delta t} &= \boldsymbol{F}^{*T}_{t+\Delta t} \boldsymbol{F}^*_{t+\Delta t} \\ \boldsymbol{E}^*_{t+\Delta t} &= \frac{1}{2} \left(\boldsymbol{C}^*_{t+\Delta t} - \boldsymbol{1} \right) \\ \boldsymbol{T}^*_{t+\Delta t} &= \boldsymbol{\mathcal{L}}[\boldsymbol{E}^*_{t+\Delta t}] \end{aligned} \tag{17}$$

The use of an implicit method ensures stability, but requires an iterative approach to solve for $\boldsymbol{F}^*_{t+\Delta t}$ using equation (14). A Newton-Raphson scheme was deemed to be the most efficient method for this purpose. Equation (14) is rewritten in the form of a residual, which at the k^{th} iteration is given by

$$\boldsymbol{\mathcal{R}}^k = \boldsymbol{F}^*_k - \boldsymbol{F}^*_t - \Delta t\, \boldsymbol{L} \boldsymbol{F}^*_k + \Delta t\, \boldsymbol{F}^*_k \left(\sum_\alpha \dot{\gamma}^\alpha_k \tilde{\boldsymbol{P}}^\alpha \right) \tag{18}$$

Note here that the subscript k has been introduced for quantities which change with iterations, and the subscript $t + \Delta t$ has been dropped from all variables for convenience. The value of $\boldsymbol{F}^*_{k+1}$ is then computed based on the Newton method as

$$\mathrm{D}\boldsymbol{\mathcal{R}}^k(\boldsymbol{F}^*_k)[\Delta \boldsymbol{F}^*_k] = -\boldsymbol{\mathcal{R}}^k \tag{19}$$

$$\boldsymbol{F}^*_{k+1} = \boldsymbol{F}^*_k + \Delta\boldsymbol{F}^*_k \tag{20}$$

Here $\mathrm{D}\boldsymbol{\mathcal{R}}^k(\boldsymbol{F}^*_k)$ is a fourth order tensor representing the derivative of $\boldsymbol{\mathcal{R}}^k$ with respect to $\boldsymbol{F}^*_k$. This derivative is rather complicated to evaluate, and it is more convenient to compute the directional derivative resulting from $\mathrm{D}\boldsymbol{\mathcal{R}}^k(\boldsymbol{F}^*_k)$ operating on $\Delta\boldsymbol{F}^*_k$. The details of this derivation are given in Appendix A, with the result that

$$\mathrm{D}\boldsymbol{\mathcal{R}}^k(\boldsymbol{F}^*_k)[\Delta\boldsymbol{F}^*_k] = \Delta\boldsymbol{F}^*_k - \Delta t\,\boldsymbol{L}\,\Delta\boldsymbol{F}^*_k + \Delta t\,\Delta\boldsymbol{F}^*_k\left(\sum_\alpha \dot\gamma^\alpha_k\,\tilde{\boldsymbol{P}}^\alpha\right) + \Delta t\,\boldsymbol{F}^*_k\,\Delta\boldsymbol{G}^*_k \tag{21}$$

$$\Delta\boldsymbol{G}^*_k = \boldsymbol{\mathcal{S}}_k[\Delta\boldsymbol{T}^*_k] \tag{22}$$

$$\boldsymbol{\mathcal{S}}_k = \sum_\alpha \frac{d\dot\gamma^\alpha_k}{d\tau^\alpha_k}(\tilde{\boldsymbol{P}}^\alpha \otimes \tilde{\boldsymbol{P}}^\alpha) \tag{23}$$

$$\Delta\boldsymbol{T}^*_k = (\Delta\boldsymbol{F}^{*T}_k\boldsymbol{F}^*_k + \boldsymbol{F}^{*T}_k\Delta\boldsymbol{F}^*_k)\boldsymbol{T}^*_k + \boldsymbol{C}^*_k\boldsymbol{\mathcal{L}}\left[\Delta\boldsymbol{F}^{*T}_k\boldsymbol{F}^*_k\right] \tag{24}$$

Combining equations (19) and (21)–(24) provides a system of equations for the nine unknown components of $\Delta\boldsymbol{F}^*_k$. The complete expressions for the Jacobian matrix and the residual are given in Appendix B. Knowing $\Delta\boldsymbol{F}^*_k$, one can compute the next approximation $\boldsymbol{F}^*_{k+1}$, and repeat this procedure until the L^2-norm of the residual $\| \boldsymbol{\mathcal{R}}^k \|$ becomes smaller than some prescribed tolerance. The initial guess for $\boldsymbol{F}^*$ is taken to be its value at the beginning of the time step. During the course of the Newton iterations, it is possible for the method to diverge, especially with larger time steps. Following the approach used by Maniatty *et al.* (1992), a scheme to limit the change in $\boldsymbol{F}^*_k$ whenever $\| \boldsymbol{\mathcal{R}}^k \|$ increases relative to the previous iteration is employed to aid convergence. The steps used at each iteration of the Newton method are as follows:

1. Compute residual $\boldsymbol{\mathcal{R}}^k$
2. Compute $\| \boldsymbol{\mathcal{R}}^k \|$
3. If $\| \boldsymbol{\mathcal{R}}^k \| <$ tolerance, exit the loop
   If $\| \boldsymbol{\mathcal{R}}^k \| > \| \boldsymbol{\mathcal{R}}^{k-1} \|$ and $k > 1$, scale back $\boldsymbol{F}^*_k$
   $$\boldsymbol{F}^*_k = \frac{1}{2}(\boldsymbol{F}^*_k + \boldsymbol{F}^*_{k-1})$$
   and go back to step 1
   If $\| \boldsymbol{\mathcal{R}}^k \| < \| \boldsymbol{\mathcal{R}}^{k-1} \|$ or $k = 1$, continue
4. Compute Jacobian and solve for $\Delta\boldsymbol{F}^*_k$
5. Compute $\boldsymbol{F}^*_{k+1} = \boldsymbol{F}^*_k + \Delta\boldsymbol{F}^*_k$

The above procedure does not automatically ensure that the determinant of $\boldsymbol{F}^*$ equals that of the deformation gradient $\boldsymbol{F}$. For this reason, it was necessary to scale the components of $\boldsymbol{F}^*$. The evolution equation for the determinant of $\boldsymbol{F}^*$ is given by

$$\frac{d}{dt}(\ln J) = \mathrm{tr}(\boldsymbol{L}) \tag{25}$$

where $J = \det(\boldsymbol{F})$ and $\boldsymbol{L}$ is the velocity gradient. This equation is integrated using a fourth-order Runge-Kutta scheme (Press *et al.*, 1990) to compute the value of $\ln J$, and hence $\det(\boldsymbol{F})$. To perform the scaling, the converged value of $\boldsymbol{F}^*$ is multiplied by the cube root of the ratio $\det(\boldsymbol{F})/\det(\boldsymbol{F}^*)$.

Upon obtaining $\boldsymbol{F}^*_{t+\Delta t}$, the hardness is updated using equation (11),

$$\hat{\tau}^\alpha_{t+\Delta t} = \hat{\tau}^\alpha_t + H_0 \left\{ \frac{\hat{\tau}_s(\dot{\gamma}^*_{t+\Delta t}) - \hat{\tau}^\alpha_t}{\hat{\tau}_s(\dot{\gamma}^*_{t+\Delta t}) - \hat{\tau}^\alpha_i} \right\} \dot{\gamma}^*_{t+\Delta t} \tag{26}$$

with $\hat{\tau}_s(\dot{\gamma}^*_{t+\Delta t})$ being computed according to equation (13).

Once $\boldsymbol{F}^*$ has been determined, its polar decomposition is used to compute the rotation $\boldsymbol{R}^*$ of the crystal lattice during the deformation,

$$\boldsymbol{F}^* = \boldsymbol{R}^* \boldsymbol{U}^* \tag{27}$$

In the integration scheme discussed above, only the integration of $\boldsymbol{F}^*$ is carried out using an implicit method. The hardness is kept constant through the Newton iterations, and is updated using an explicit step upon convergence of $\boldsymbol{F}^*$. While this is the procedure used for all the results shown in the next section, a scheme involving fully implicit integration of both $\boldsymbol{F}^*$ and $\hat{\tau}^\alpha$ has also been tested. In this method, first $\hat{\tau}^\alpha$ is kept fixed at its best estimate while solving for $\boldsymbol{F}^*$, followed by implicit integration of $\hat{\tau}^\alpha$ with the updated value of $\boldsymbol{F}^*$. These iterations are repeated until both $\boldsymbol{F}^*$ and $\hat{\tau}^\alpha$ converge to the required tolerance. It was found that the results from this fully implicit method were not significantly different from those obtained with explicit update of the hardness. Since several sets of iterations are required by the fully implicit scheme, the simulation time for the two level iterative scheme was quite large while the corresponding gain in accuracy was minimal.

4 Numerical Results

The integration procedure described in the previous section has been used to simulate the texture evolution and stress-strain response of an aggregate of 1000 crystals with initially uniform distribution of orientations. The initial texture is depicted in Fig. 2 in the form of <100> and <111> pole figures. Crystal orientations in the form of Euler angles (Kocks, 1988) were processed using the DIOR program of popLA (Kallend *et al.*, 1991), and the resulting contours were subjected to 5° Gaussian smoothing in order to generate the pole figures. The velocity gradient of each crystal was assumed to be the same as the applied velocity gradient under the extended Taylor hypothesis (Taylor, 1938; Asaro and Needleman, 1985). The average of the crystal stresses was taken to be the stress in the polycrystalline aggregate.

Numerical simulations were carried out with two different crystal structures. For the first set of runs, the crystals were assumed to be face centered cubic, deforming on the {111} <110> slip systems, with material parameters for 1100 aluminum (Mathur and Dawson, 1989) shown in Table 1. The tolerance for convergence of the Newton iterations was

Table 1: Parameters for the polycrystal simulations with FCC material.

Parameter	Value	Units
μ	25.3	GPa
λ	54.4	GPa
m	0.05	
$\dot{\gamma}_0$	1.0	s^{-1}
H_0	58.41	MPa
$\hat{\tau}_i^\alpha$	27.17	MPa
τ_{s0}	61.8	MPa
$\dot{\gamma}_s$	5.0×10^{10}	s^{-1}
m'	0.005	

taken to be 10^{-12}. The elastic response was assumed to be isotropic, so that the elasticity tensor takes the form

$$\boldsymbol{\mathcal{L}} = 2\mu\mathfrak{S} + \lambda(\mathbf{1}\otimes\mathbf{1})$$

where μ and λ are Lamé's constants, and $\mathfrak{S}$ and $\mathbf{1}$ are the symmetric fourth order and second order identity tensors, respectively.

The effect of the time step was examined first by deforming the crystals in tension with a velocity gradient (in s^{-1}) given by

$$[L] = \begin{bmatrix} 1.0 & 0.0 & 0.0 \\ 0.0 & -0.5 & 0.0 \\ 0.0 & 0.0 & -0.5 \end{bmatrix}$$

using three different time increments. Deformation to a strain of 2.0 was simulated using times steps of 0.05, 0.01 and 0.001. Figure 3 shows the von Mises effective stress normalized by the initial slip system hardness as a function of effective strain for the three time steps. It is seen that the stress-strain response predicted for the two smaller time increments is very similar, with the largest time step leading to greater deviation. The difference between the curves is larger at smaller values of strain, but becomes minimal as the stress reaches its saturation value due to the nature of the evolution equation for the hardness (Maniatty *et al.*, 1992). The textures predicted using different time steps are all very similar, as illustrated in Fig. 4. The <100> pole figures in a projection normal to the tensile axis obtained using $\Delta t = 0.001$ and 0.05 show very little difference.

The model presented here has been compared with a rigid-viscoplastic model based on the Taylor hypothesis (Mathur and Dawson, 1989), in which the elastic response of the material is neglected. The stress-strain response from the two models is shown in Fig. 5, with very similar predictions by the two models. The elasto-viscoplastic model predicts the initial elastic response, whereas the rigid-viscoplastic starts from a non-zero stress in response to the instantaneous applied strain rate. The textures from the two models are compared in Fig. 6, and the differences between the <100> pole figures are negligible.

Table 2: Elastic constants for zirconium.

Parameter	Value	Units
c_{11}	143.5	GPa
c_{12}	72.5	GPa
c_{13}	65.4	GPa
c_{33}	164.9	GPa
c_{44}	32.1	GPa

The polycrystalline aggregate was also deformed in plane strain compression using a velocity gradient (in s^{-1})

$$[L] = 0.8660254 \begin{bmatrix} 1.0 & 0.0 & 0.0 \\ 0.0 & 0.0 & 0.0 \\ 0.0 & 0.0 & -1.0 \end{bmatrix}$$

with the leading factor chosen to give a unit effective strain rate. Deformation to a strain of 2.0 was simulated using a time increment of 0.01. The stress-strain response from the elasto-viscoplastic and rigid-viscoplastic models showed results similar to the case of deformation in tension. The texture predictions in the form of <111> pole figures in a projection normal to the compression axis are plotted in Fig. 7, and show typical rolling texture components predicted by a Taylor simulation (Hirsch and Lücke, 1988; Sarma and Dawson, 1996b).

In order to highlight the capability of the model to capture elastic effects, the model has been used to simulate a process where the aggregate of crystals is deformed first in tension to a strain of 0.1, at which point the velocity gradient is instantaneously reversed. When the strain becomes 0.02, the deformation is again reversed to tension. The resulting stress-strain response is shown in Fig. 8, and clearly indicates the elastic unloading and the subsequent plastic deformation during load reversal. The increase in yield stress due to hardening of slip systems is also apparent.

The results presented so far have been for a material with FCC crystal structure. Applicability of the elasto-viscoplastic model to other crystal types is demonstrated through an example using HCP crystals. Single crystals of zirconium with different initial orientations were deformed in plane strain compression to a strain of 2%. Deformation was assumed to occur on the three $\{10\bar{1}0\}$ $<1\bar{2}10>$ prismatic and twelve $\{10\bar{1}1\}$ $<11\bar{2}3>$ pyramidal slip systems (Turner *et al.*, 1995). The slip system hardness values were assumed to remain constant at 110 MPa and 200 MPa for the prismatic and pyramidal systems, respectively, since the total strain is small. Rate sensitivity m was taken to be 0.05. Five elastic constants are needed to describe the elastic response of hexagonal crystals (Hertzberg, 1989). The anisotropic elastic response of zirconium was modeled using the constants shown in Table 2 (Fisher and Renken, 1961). The resulting stress-strain curves for three crystals are shown in Fig. 9. The effect of anisotropy in the elastic response is clearly seen from the slopes of the linear portion. The anisotropy in properties will have significant influence on the residual stress distribution in a polycrystalline aggregate. In contrast, the stress-strain

response obtained assuming isotropic elasticity (with $\mu = 32.1$ GPa and $\lambda = 72.5$ GPa) is plotted in Fig. 10 and shows similar behavior for the three crystals up to the yield point.

5 Conclusions

A novel integration scheme for modeling the elasto-viscoplastic response of polycrystalline materials is presented and applied to model texture evolution and stress-strain response. The model is based on multiplicative decomposition of the crystal deformation gradient into plastic and elastic parts. The elastic deformation gradient also incorporates the rigid rotation of the crystal. It is shown that prescribing the deformation of the crystal in terms of its velocity gradient leads to an expression for the evolution of the elastic deformation gradient. This form is well suited for use in a velocity based finite element formulation, where the velocity gradient at each integration point is known, and the stress must be evaluated. The form of the equation is simple and direct, since the integration of this equation provides information about the elastic strain as well as the reorientation of the crystal. An implicit scheme to integrate the evolution equation for the elastic deformation gradient has been described. The backward Euler update utilizes the Newton-Raphson method to allow for stable and efficient integration even with large time steps.

Numerical examples have been presented to demonstrate the general nature of the model and its applicability to various crystal types. The texture predictions using the elasto-viscoplastic model do not differ significantly from those obtained using a rigid-viscoplastic model which ignores elasticity. This is as expected, since the reorientation of crystals is a consequence of plastic deformation. The stress-strain behavior also shows little difference except in the initial elastic portion. If the interest is in large strain texture and stress response, then ignoring the elastic component is a valid assumption. However, in situations which require the elastic component, such as prediction of residual stresses or springback during sheet forming applications, the model presented here would prove to be a useful tool.

Acknowledgments

This research was sponsored by the U.S. Navy, Office of Naval Research under interagency agreement DOE No. 1866-E126-A1, Navy No. N000014-92-F-0063, and by the Division of Materials Science, U.S. Department of Energy, under contract DE-AC05-96OR22464 with Lockheed Martin Energy Research Corporation. The research was supported in part by an appointment to the Oak Ridge National Laboratory Postdoctoral Research Associates Program administered jointly by the Oak Ridge National Laboratory and the Oak Ridge Institute for Science and Education. The authors are grateful to one of the referees for valuable suggestions to improve the integration method.

References

Asaro, R. J. and Needleman, A. (1985) Texture development and strain hardening in rate dependent polycrystals. *Acta Metall.* **33**, 923–953.

Balasubramanian, S. and Anand, L. (1996) Single crystal and polycrystal elasto-visco-plasticity: Application to earing in cup drawing of F.C.C. materials. *Comp. Mech.* **17**, 209–225.

Beaudoin, A. J., Dawson, P. R., Mathur, K. K., Kocks, U. F. and Korzekwa, D. A. (1994) Application of polycrystal plasticity to sheet forming. *Comput. Methods Appl. Mech. Engrg.* **117**, 49–70.

Beaudoin, A. J., Mecking, H. and Kocks, U. F. (1996) Development of localized orientation gradients in fcc polycrystals. *Phil. Mag. A* **73**, 1503–1517.

Becker, R. (1991a) Applications of crystal plasticity constitutive models. In *Modeling the Deformation of Crystalline Solids*, ed. T. C. Lowe, A. D. Rollett, P. S. Follansbee and G. S. Daehn, pp. 249–269. TMS, Warrendale, PA.

Becker, R. (1991b) Analysis of texture evolution in channel die compression—I. Effects of grain interaction. *Acta Metall.* **39**, 1211–1230.

Bronkhorst, C. A., Kalidindi, S. R. and Anand, L. (1992) Polycrystalline plasticity and the evolution of crystallographic texture in FCC metals. *Phil. Trans. R. Soc. Lond.* A **341**, 443–477.

Dawson, P., Beaudoin, A., Mathur, K. and Sarma, G. (1994) Finite element modeling of polycrystalline solids. *European J. Finite Elements* **3**, 543–571.

Fisher, E. S. and Renken, C. J. (1961) Adiabatic elastic moduli of single crystal alpha zirconium. *J. Nucl. Mater.* **4**, 311–315.

Gurtin, M. E. (1981) *An introduction to continuum mechanics.* Academic Press, New York.

Hertzberg, R. W. (1989) *Deformation and fracture mechanics of engineering materials.* John Wiley & Sons, New York.

Hirsch, J. and Lücke, K. (1988) Mechanism of deformation and development of rolling textures in polycrystalline F.C.C. metals—II. Simulation and interpretation of experiments on the basis of Taylor-type theories. *Acta Metall.* **36**, 2883–2904.

Hutchinson, J. W. (1976) Bounds and self-consistent estimates for creep of polycrystalline materials. *Proc. R. Soc. Lond. A* **348**, 101–127.

Kalidindi, S. R., Bronkhorst, C. A. and Anand, L. (1992) Crystallographic texture evolution in bulk deformation processing of FCC metals. *J. Mech. Phys. Solids* **40**, 537–569.

Kallend, J. S., Kocks, U. F., Rollett, A. D. and Wenk, H. -R. (1991) Operational texture analysis. *Mater. Sci. Engrg. A* **132**, 1–11.

Kocks, U. F. (1976) Laws for work-hardening and low-temperature creep. *J. Eng. Mater. Tech.* **98**, 76–85.

Kocks, U. F. (1987) Constitutive behavior based on crystal plasticity. In *Unified Constitutive Equations for Creep and Plasticity*, ed. A. K. Miller, pp. 1–88. Elsevier Applied Science, New York.

Kocks, U. F. (1988) A symmetric set of Euler angles and oblique orientation sections. In *Proc. Eighth Inter. Conf. on Textures of Mater. (ICOTOM 8)* ed. J. S. Kallend and G. Gottstein, pp. 31–36. TMS, Warrendale, PA.

Lee, E. H. (1969) Elastic-plastic deformation at finite strains. *J. Appl. Mech.* **36**, 1–6.

Maniatty, A. M., Dawson, P. R. and Lee, Y. -S. (1992) A time integration algorithm for elasto-viscoplastic cubic crystals applied to modeling polycrystalline deformation. *Inter. J. Num. Meth. Engrg.* **35**, 1565–1588.

Mathur, K. K. and Dawson, P. R. (1989) On modeling the development of crystallographic texture in bulk forming processes. *Int. J. Plast.* **5**, 67–94.

Mathur, K. K., Dawson, P. R. and Kocks, U. F. (1990) On modeling anisotropy in deformation processes involving textured polycrystals with distorted grain shape. *Mech. Mater.* **10**, 183–202.

Pan, J. and Rice, J. R. (1983) Rate sensitivity of plastic flow and implications for yield surface vertices. *Int. J. Solids Struct.* **19**, 973–987.

Peirce, D., Asaro, R. J. and Needleman, A. (1983) Material rate dependence and localized deformation in crystalline solids. *Acta Metall.* **31**, 1951–1976.

Press, W. H., Flannery, B. P., Teukolsky, S. A. and Vetterling, W. T. (1990) *Numerical recipes in C*. Cambridge University Press, New York.

Rice, J. R. (1971) Inelastic constitutive relations for solids: an internal-variable theory and its application to metal plasticity. *J. Mech. Phys. Solids* **19**, 433–455.

Sarma, G. B. and Dawson, P. R. (1996a) Effects of interactions among crystals on the inhomogeneous deformations of polycrystals. *Acta mater.* **44**, 1937–1953.

Sarma, G. B. and Dawson, P. R. (1996b) Texture predictions using a polycrystal plasticity model incorporating neighbor interactions. *Int. J. Plast.* **12**, 1023–1054.

Sarma, G. B., Radhakrishnan, B. and Zacharia, T. (1998) Finite element simulations of cold deformation at the mesoscale. *Comp. Mater. Sci.* in press.

Taylor, G. I. (1938) Plastic strain in metals. *J. Inst. Metals* **62**, 307–324.

Turner, P. A., Christodoulou, N. and Tomé, C. (1995) Modeling the mechanical response of rolled Zircaloy-2. *Int. J. Plast.* **11**, 251–265.

Appendix

A Directional derivative

The residual at the k^{th} iteration of the Newton method is given by equation (18). Expressing $\boldsymbol{\mathcal{R}}^{k+1}$ about $\boldsymbol{F}^*_{k+1}$ in a Taylor series, and neglecting higher order terms yields

$$\boldsymbol{\mathcal{R}}^{k+1} = \boldsymbol{\mathcal{R}}^{k} + \mathrm{D}\boldsymbol{\mathcal{R}}^{k}(\boldsymbol{F}^*_k)[\boldsymbol{F}^*_{k+1} - \boldsymbol{F}^*_k] \tag{28}$$

Setting the left hand side to zero leads to equation (19). Applying the rules of tensor differentiation (Gurtin, 1981), and recognizing that $\boldsymbol{F}^*_t$, $\boldsymbol{L}$ and $\tilde{\boldsymbol{P}}^{\alpha}$ are independent of $\boldsymbol{F}^*_k$, the directional derivative is given by

$$\mathrm{D}\boldsymbol{\mathcal{R}}^{k}[\Delta\boldsymbol{F}^*_k] = \Delta\boldsymbol{F}^*_k - \Delta t\,\boldsymbol{L}\,\Delta\boldsymbol{F}^*_k + \Delta t\,\Delta\boldsymbol{F}^*_k\left(\sum_{\alpha}\dot{\gamma}^{\alpha}_k\tilde{\boldsymbol{P}}^{\alpha}\right) + \Delta t\,\boldsymbol{F}^*_k\left(\sum_{\alpha}\tilde{\boldsymbol{P}}^{\alpha}\mathrm{D}\dot{\gamma}^{\alpha}_k[\Delta\boldsymbol{F}^*_k]\right) \tag{29}$$

Using equation (15), the last term in the above expression involving the derivative of $\dot{\gamma}^{\alpha}_k$ may be written as

$$\begin{aligned}
\Delta\boldsymbol{G}^*_k &= \sum_{\alpha}\tilde{\boldsymbol{P}}^{\alpha}\mathrm{D}\dot{\gamma}^{\alpha}_k[\Delta\boldsymbol{F}^*_k] \\
&= \sum_{\alpha}\tilde{\boldsymbol{P}}^{\alpha}\frac{d\dot{\gamma}^{\alpha}_k}{d\tau^{\alpha}_k}\mathrm{D}\tau^{\alpha}_k[\Delta\boldsymbol{F}^*_k] \\
&= \sum_{\alpha}\tilde{\boldsymbol{P}}^{\alpha}\frac{\dot{\gamma}_0}{m\hat{\tau}^{\alpha}_t}\left|\frac{\tau^{\alpha}_k}{\hat{\tau}^{\alpha}_t}\right|^{\frac{1}{m}-1}\mathrm{D}\tau^{\alpha}_k[\Delta\boldsymbol{F}^*_k]
\end{aligned} \tag{30}$$

The derivative with respect to the resolved shear stress can be obtained from equations (16) and (17). Writing τ^{α}_k as a function of $\boldsymbol{F}^*_k$,

$$\tau^{\alpha}_k = \left\{(\boldsymbol{F}^{*T}_k\boldsymbol{F}^*_k)\,\boldsymbol{\mathcal{L}}\left[(1/2)(\boldsymbol{F}^{*T}_k\boldsymbol{F}^*_k - \mathbf{1})\right]\right\}\cdot\tilde{\boldsymbol{P}}^{\alpha} \tag{31}$$

where $\boldsymbol{\mathcal{L}}$ is the fourth order elasticity tensor, the directional derivative is computed to be

$$\begin{aligned}
\mathrm{D}\tau^{\alpha}_k[\Delta\boldsymbol{F}^*_k] &= \left\{(\Delta\boldsymbol{F}^{*T}_k\boldsymbol{F}^*_k + \boldsymbol{F}^{*T}_k\Delta\boldsymbol{F}^*_k)\,\boldsymbol{\mathcal{L}}\left[(1/2)(\boldsymbol{F}^{*T}_k\boldsymbol{F}^*_k - \mathbf{1})\right]\right\}\cdot\tilde{\boldsymbol{P}}^{\alpha} \\
&+ \left\{(\boldsymbol{F}^{*T}_k\boldsymbol{F}^*_k)\boldsymbol{\mathcal{L}}\left[(1/2)(\Delta\boldsymbol{F}^{*T}_k\boldsymbol{F}^*_k + \boldsymbol{F}^{*T}_k\Delta\boldsymbol{F}^*_k)\right]\right\}\cdot\tilde{\boldsymbol{P}}^{\alpha}
\end{aligned}$$

Making use of equations (4) and (5), and the symmetries of the elasticity tensor $\boldsymbol{\mathcal{L}}$, the above directional derivative can be rewritten as

$$\mathrm{D}\tau^{\alpha}_k[\Delta\boldsymbol{F}^*_k] = \Delta\boldsymbol{T}^*_k\cdot\tilde{\boldsymbol{P}}^{\alpha} \tag{32}$$

where

$$\Delta \boldsymbol{T}_k^* = (\Delta \boldsymbol{F}_k^{*T} \boldsymbol{F}_k^* + \boldsymbol{F}_k^{*T} \Delta \boldsymbol{F}_k^*) \boldsymbol{T}_k^* + \boldsymbol{F}^{*T}_k \boldsymbol{F}_k^* \boldsymbol{\mathcal{L}} \left[\Delta \boldsymbol{F}_k^{*T} \boldsymbol{F}_k^* \right] \tag{33}$$

Substituting equation (32) into equation (30) provides a compact expression for $\Delta \boldsymbol{G}_k^*$,

$$\Delta \boldsymbol{G}_k^* = \sum_\alpha \tilde{\boldsymbol{P}}^\alpha \frac{d\dot{\gamma}_k^\alpha}{d\tau_k^\alpha} (\Delta \boldsymbol{T}_k^* \cdot \tilde{\boldsymbol{P}}^\alpha) \tag{34}$$

which can be rewritten as

$$\Delta \boldsymbol{G}_k^* = \left\{ \sum_\alpha \frac{d\dot{\gamma}_k^\alpha}{d\tau_k^\alpha} \tilde{\boldsymbol{P}}^\alpha \otimes \tilde{\boldsymbol{P}}^\alpha \right\} [\Delta \boldsymbol{T}_k^*] = \boldsymbol{\mathcal{S}}_k [\Delta \boldsymbol{T}_k^*] \tag{35}$$

where $\Delta \boldsymbol{T}_k^*$ is defined in equation (33).

B Jacobian for the Newton-Raphson method

In order to set up a system of equations for computing the nine components of $\Delta \boldsymbol{F}_k^*$, it is necessary to form a Jacobian matrix of coefficients. To this end, it is desirable to rewrite equation (19) in indicial notation as

$$D_{ijkl}\, \Delta F_{kl}^* = -R_{ij} \tag{36}$$

where the subscript k no longer denotes iteration number, but ranges from 1 to 3 along with the other indices. From equation (21),

$$D_{ijkl}\, \Delta F_{kl}^* = \Delta F_{ij}^* - \Delta t\, L_{im}\, \Delta F_{mj}^* + \Delta t\, \Delta F_{im}^*\, \tilde{L}_{mj}^p + \Delta t\, F_{im}^*\, \Delta G_{mj}^* \tag{37}$$

The contribution from the first three terms on the right hand side of the above equation can be written as

$$\begin{aligned} D^0_{ijkl}\, \Delta F_{kl}^* &= \Delta F_{ij}^* - \Delta t\, L_{im}\, \Delta F_{mj}^* + \Delta t\, \Delta F_{im}^*\, \tilde{L}_{mj}^p & (38) \\ &= \delta_{ik}\, \delta_{jl}\, \Delta F_{kl}^* - \Delta t\, L_{ik}\, \delta_{jl}\, \Delta F_{kl}^* + \Delta t\, \Delta F_{kl}^*\, \tilde{L}_{lj}^p\, \delta_{ik} & (39) \end{aligned}$$

so that

$$D^0_{ijkl} = \delta_{ik}\, \delta_{jl} - \Delta t\, L_{ik}\, \delta_{jl} + \Delta t\, \delta_{ik}\, \tilde{L}_{lj}^p \tag{40}$$

Contribution from the last term on the right hand side of equation (37) is given by

$$\Delta t\, F_{ip}^*\, \Delta G_{pj}^* = \Delta t\, F_{ip}^*\, \mathcal{S}_{pjln}\, \Delta T_{ln}^*$$

From equation (24), it is seen that the contribution from $\Delta \boldsymbol{T}_k^*$ can be separated into three terms. Taking each term in turn,

$$D^1_{ijkl}\, \Delta F_{kl}^* = \Delta t\, F_{ip}^*\, \mathcal{S}_{pjln}\, \Delta F_{kl}^*\, F_{kt}^*\, T_{tn}^* \tag{41}$$

$$D^2_{ijkl}\, \Delta F_{kl}^* = \Delta t\, F_{ip}^*\, \mathcal{S}_{pjmn}\, F_{km}^*\, \Delta F_{kl}^*\, T_{ln}^* \tag{42}$$

$$D^3_{ijkl}\, \Delta F_{kl}^* = \Delta t\, F_{ip}^*\, \mathcal{S}_{pjmn}\, C_{mq}^*\, \mathcal{L}_{qnls}\, \Delta F_{kl}^*\, F_{ks}^* \tag{43}$$

Finally, the components of the Jacobian are obtained using equations (40)–(43) by the following addition

$$D_{ijkl} = D^0_{ijkl} + D^1_{ijkl} + D^2_{ijkl} + D^3_{ijkl} \tag{44}$$

List of Figures

1 Schematic of single crystal kinematics showing multiplicative decomposition. 17
2 <100> and <111> pole figures in equal area projection showing initial texture of the crystals. Contour levels represent multiples of random texture intensity. 18
3 Effective stress normalized by initial hardness plotted against effective strain for tensile deformation simulated using different time increments. 19
4 <100> pole figures in equal area projection showing texture after tensile deformation predicted using different time increments. 20
5 Effective stress normalized by initial hardness plotted against effective strain for tensile deformation simulated using two different models. 21
6 <100> pole figures in equal area projection showing texture after tensile deformation predicted using two different models. 22
7 <111> pole figures in equal area projection showing texture after plane strain compression predicted using two different models. 23
8 Deviatoric stress along tensile/compressive axis normalized by initial hardness plotted against effective strain from simulation of reverse loading. 24
9 Effective stress normalized by initial hardness plotted against effective strain for three zirconium crystals at different orientations assuming anisotropic elasticity. 25
10 Effective stress normalized by initial hardness plotted against effective strain for three zirconium crystals at different orientations assuming isotropic elasticity. 26

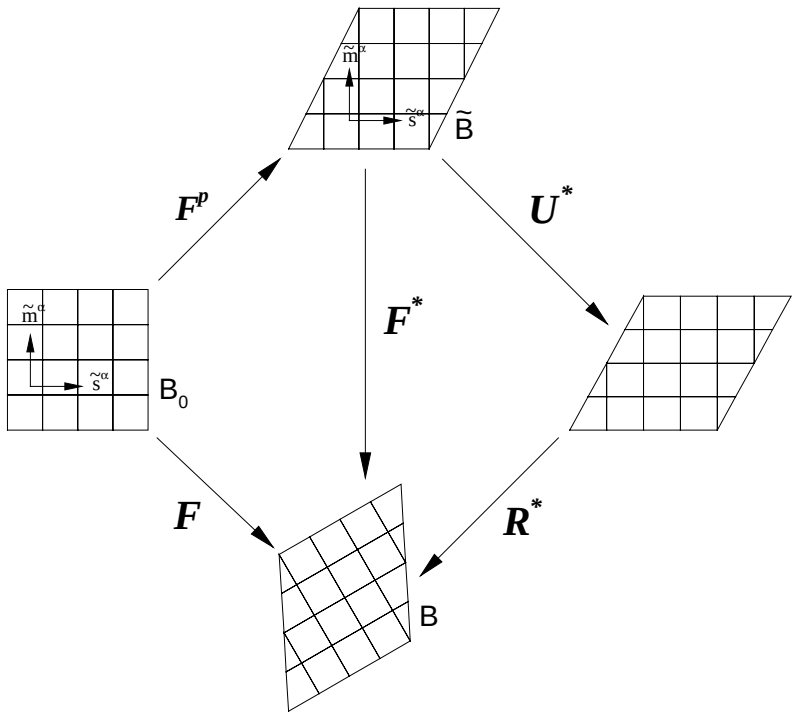

Figure 1: Schematic of single crystal kinematics showing multiplicative decomposition.

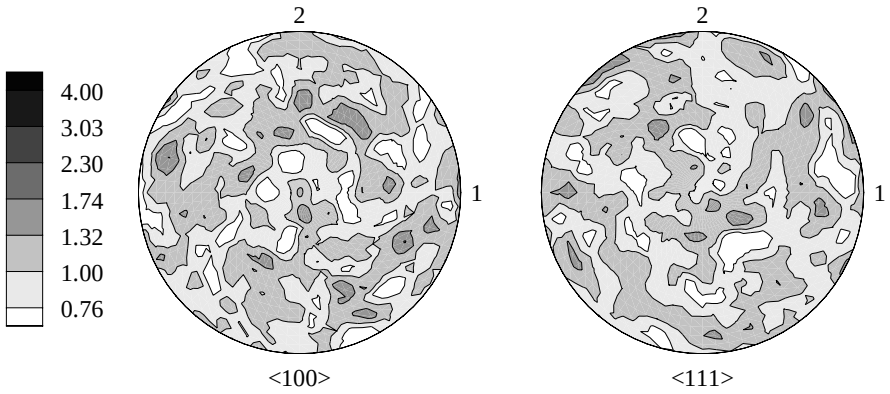

Figure 2: <100> and <111> pole figures in equal area projection showing initial texture of the crystals. Contour levels represent multiples of random texture intensity.

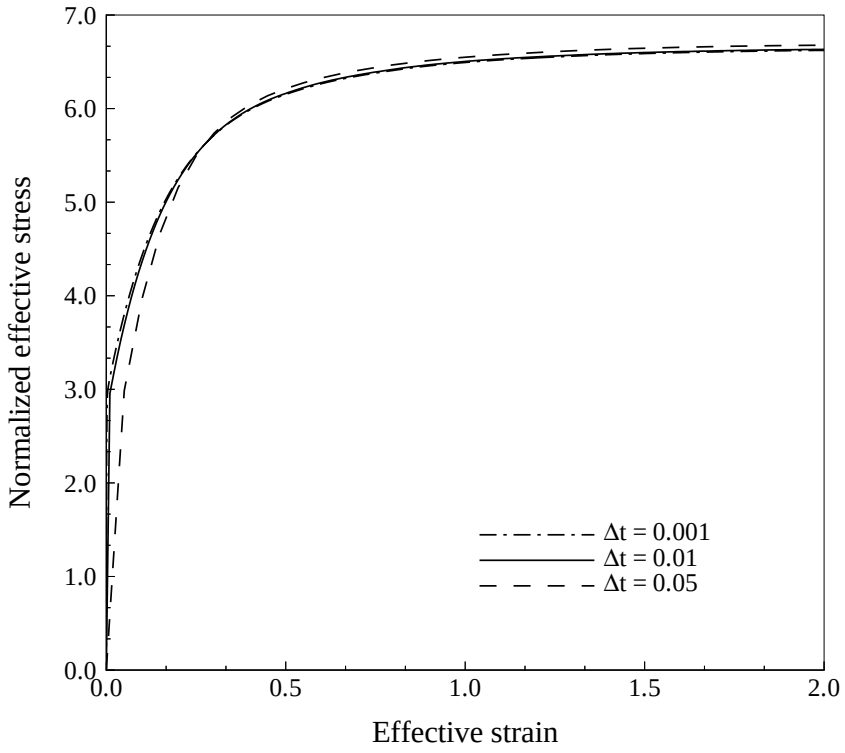

Figure 3: Effective stress normalized by initial hardness plotted against effective strain for tensile deformation simulated using different time increments.

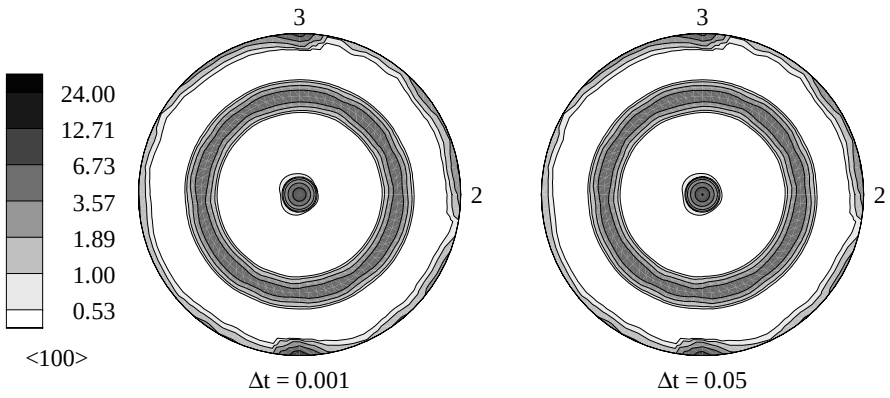

Figure 4: <100> pole figures in equal area projection showing texture after tensile deformation predicted using different time increments.

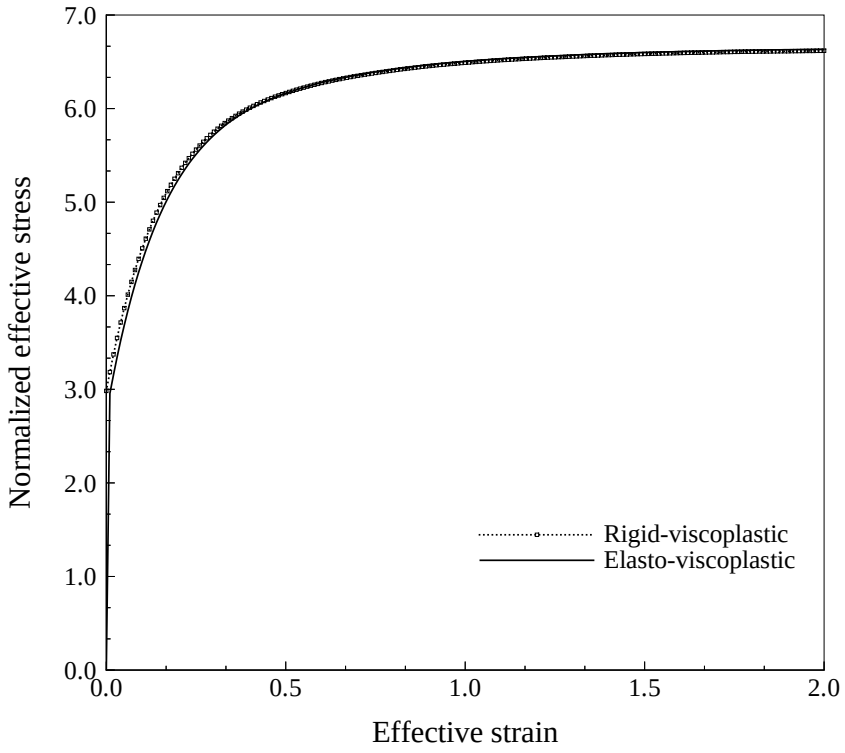

Figure 5: Effective stress normalized by initial hardness plotted against effective strain for tensile deformation simulated using two different models.

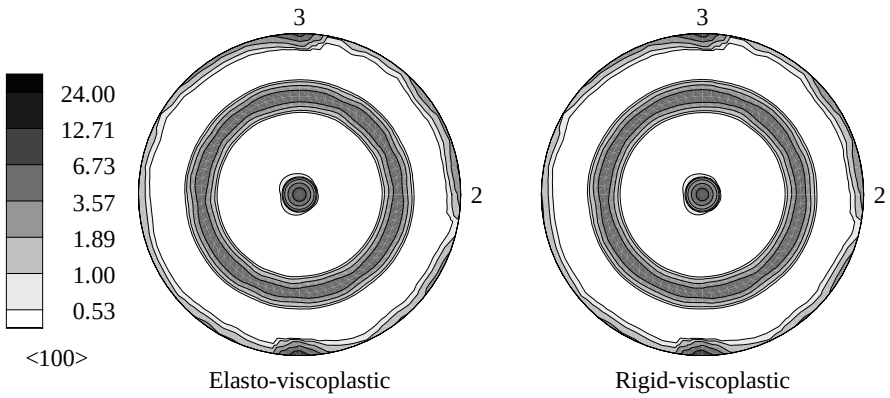

Figure 6: <100> pole figures in equal area projection showing texture after tensile deformation predicted using two different models.

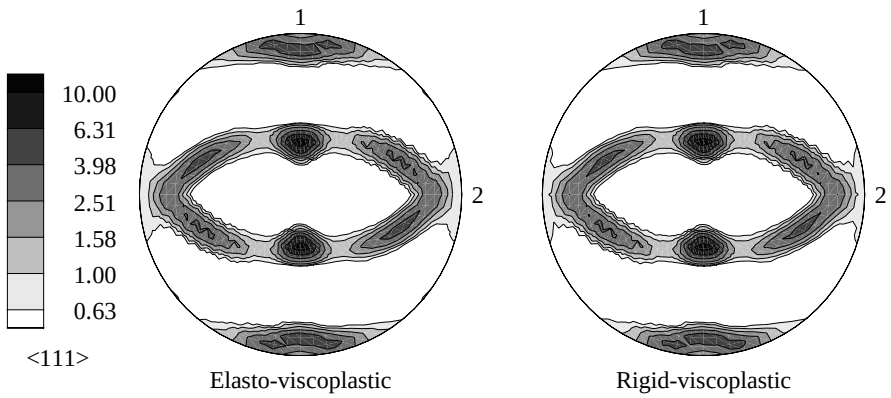

Figure 7: <111> pole figures in equal area projection showing texture after plane strain compression predicted using two different models.

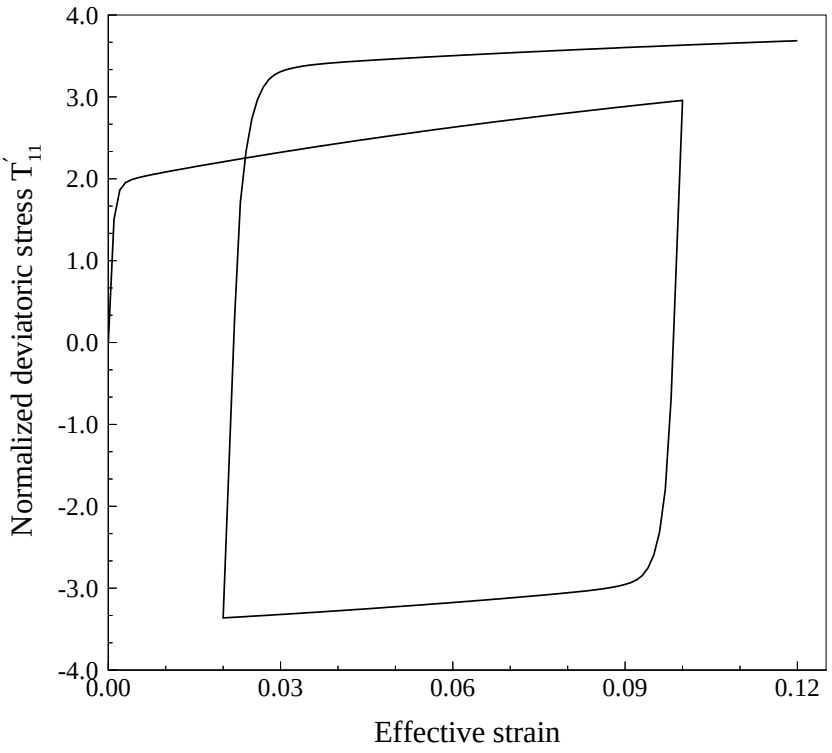

Figure 8: Deviatoric stress along tensile/compressive axis normalized by initial hardness plotted against effective strain from simulation of reverse loading.

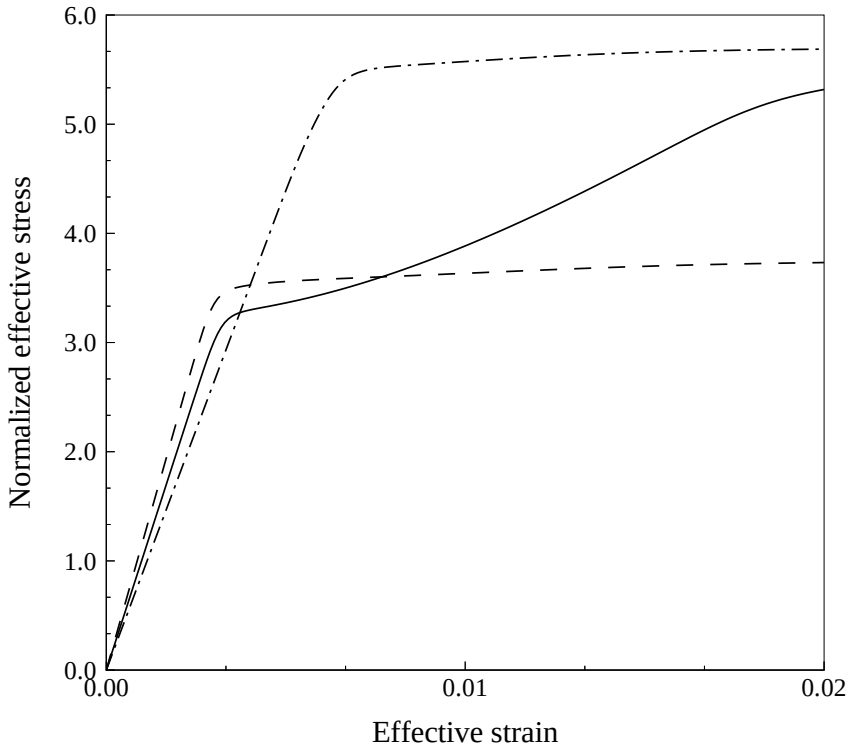

Figure 9: Effective stress normalized by initial hardness plotted against effective strain for three zirconium crystals at different orientations assuming anisotropic elasticity.

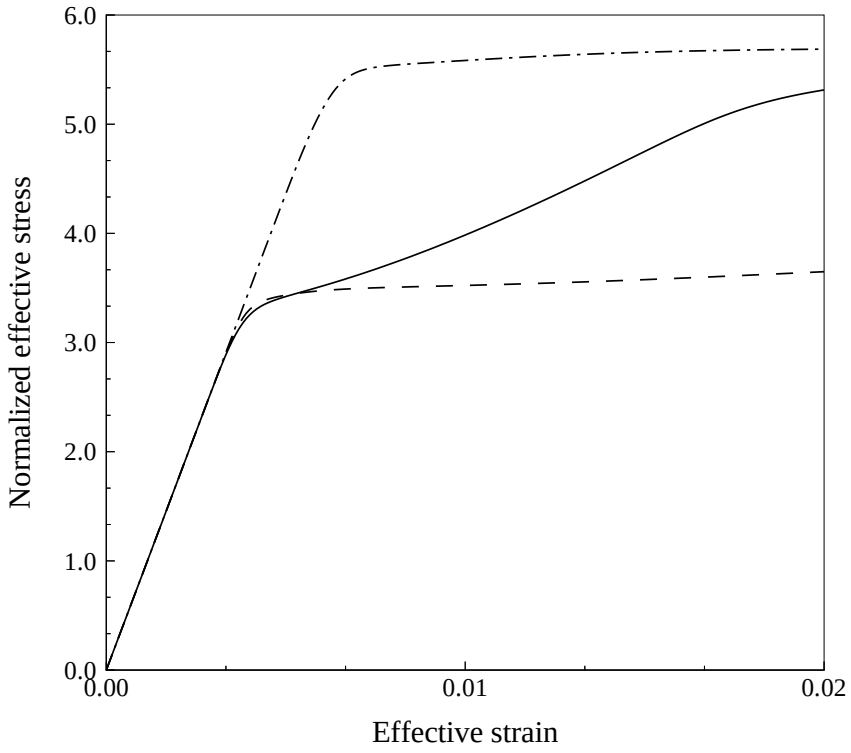

Figure 10: Effective stress normalized by initial hardness plotted against effective strain for three zirconium crystals at different orientations assuming isotropic elasticity.